

Effect of Feedstock Powder Morphology on Cold-Sprayed Titanium Dioxide Coatings

H. Hajipour¹ · A. Abdollah-zadeh¹ · H. Assadi² · E. Taheri-Nassaj¹ · H. Jahed³

Submitted: 23 July 2018 / in revised form: 23 September 2018 / Published online: 2 November 2018
© ASM International 2018

Abstract The properties of cold-sprayed ceramic coatings depend not only on the process parameters but also on the feedstock powder characteristics. To clarify the effect of feedstock powder on cold spraying, two titanium oxide powders were used in this study: (1) nanopowder and (2) agglomerated powder prepared with nanoparticles and polyvinyl alcohol. The cross sections of the deposited coatings were observed by scanning electron microscopy (SEM). The results showed that the agglomerated powder with micrometer particles made of nano-sized particles passes successfully through the bow shock layer and reached the substrate, thus forming a coating. These particles are embedded into the substrate and form a strong interfacial coating/substrate bond. SEM images revealed that the metallic substrate undergoes plastic deformation, providing interlocking with the particles of the powder, and hence, reasonable bonding to the substrate.

Keywords agglomerated powder · cold spray · nanopowder · powder particle morphology · TiO₂ coating

Introduction

The cold spray (CS) process, also known as cold gas dynamic spray, is a relatively new solid-state coating technique based on the high-speed impact of metals and ceramic particles on different substrates. A coating can be fabricated at low temperature. Unlike those in conventional thermal spray techniques, process gas temperatures are low enough and exposures to the hot gas stream are short enough to avoid melting of the particles (Ref 1-4). CS method can be considered a safe and green technology because of the absence of high-temperature explosive gases and radiation. Currently, it is being used also as an additive manufacturing process for geometrical and/or structural restoration of defected parts (Ref 5).

The higher particle velocity and lower processing temperature in CS produce a series of advantages compared to other coating techniques like thermal spray, sol-gel, sputtering. The oxidation, grain growth and phase transformation can be avoided because of the limited heat effects on substrates and spray powders. Therefore, it is possible to deposit phase transformation-sensitive materials (Ref 6-10), oxidation-sensitive materials (Ref 11-14) and also use an expanded range of substrates such as metals, ceramics and polymers (Ref 15, 16). In addition, the resulting residual stresses in coatings are normally relatively low and mostly compressive compared to those in thermal spray, which permits the deposition of thick coating with lower porosity (Ref 17, 18). CS has a high deposition efficiency and high deposition rate and does not need a high-temperature heat source. Another advantage is that the substrate needs no surface preparation to achieve good deposition. During the initial deposition stage, due to the high kinetic energy of the powder in the spray process, the particles impacting the substrate will act as cleaning agents

✉ A. Abdollah-zadeh
zadeh100@yahoo.com; zadeh@modares.ac.ir

¹ Department of Materials Engineering, Tarbiat Modares University, Tehran, Iran

² Brunel Centre for Advanced Solidification Technology (BCAST), Brunel University London, Uxbridge, UK

³ Department of Mechanical and Mechatronics Engineering, University of Waterloo, Waterloo, Canada

in a way similar to sand blasting. Surface contaminants such as dirt, oils and native oxide layers are removed by the initial particle collisions (Ref 19, 20).

In the last decade, much work has been done to explore the bonding mechanism during the CS process (Ref 21, 22). The accepted hypothesis on the bonding process is that a coating is formed through the intensive plastic deformation of particles impacting a substrate at a temperature well below the melting point of the spray material. The bonding of cold-sprayed particles is associated with adiabatic shear instability, leading to large plastic strains, and occurs beyond a certain velocity (Ref 19, 23). At impact velocities above the critical velocity, a large proportion of the impact energy is converted to heat. Therefore, the temperature in the contact area rises rapidly which leads to viscoplastic material flow away from the impact site (Ref 24). This jet cleans the oxide film off particles and substrate surfaces, increasing their activity for metallurgical bonding.

The CS process is most typically applied to metallic powder but not to ceramic ones because of their brittle characteristic (Ref 25). A brittle ceramic would not go through plastic deformation but would instead break. However, several studies have shown the ability to fabricate a ceramic coating such as TiO₂, by cold spray. There is a specific interest in the deposition of TiO₂ coating by CS, as this technology would overcome the undesirable anatase to rutile phase transformation issues of TiO₂ coating. In 2004, Ballhorn et al. (Ref 26) initially reported on using CS to embed anatase particles in a plastic surface. The particles penetrated the polymer and provided a certain area of metal oxide on the surface, which was intended to enable the photocatalytic degradation of contaminants. Later, in 2007, Klassen and Kliemann (Ref 27) used TiO₂ powder mixed with a ductile metallic powder to manufacture a photocatalytic coating by cold spray process. With this mixture, only 30–80% of metal oxide particles appear on the top surface of the coating, which may limit the final performance of the photocatalyst. Yang et al. (Ref 28) deposited nano-TiO₂ powder, which had already been agglomerated by using an organic binder. The powder after agglomeration is relatively spherical with the size in a range of 10–45 μm. During CS process, the TiO₂ powder impacts on a substrate surface at a high velocity and the spherical powder deform under high transient impact pressure due to the presence of organic binder in agglomerated particles. Although this organic binder can help improve the adhesion of the coating to the substrate, but coating includes certain impurities such as a binder material, which is quite undesirable for the photocatalytic application of the TiO₂ coating. After that, Kliemann et al. (Ref 29) investigated the formation of TiO₂ coating on four different metal substrate types. The TiO₂ particles ranged

from about 3 to 50 μm and were cold-sprayed using nitrogen as a processing gas with an inlet pressure of 4.0 MPa. The spray particles did not build up a coating because of their brittleness and high pressure of the coating process. Due to fracture under the elastic rebound forces, the brittle sprayed particles broke, and only small remnants remained on the substrate. As a result, the researchers were unable to fabricate uniform TiO₂ ceramic coating by cold spray.

In 2010, Yamada et al. (Ref 30) reported successful titanium oxide film production by cold gas spraying and also showed that no modification to the cold spray equipment was needed. During the spraying, they changed process parameters such as the nature of the gas, the pressure and the temperature in order to understand whether they were important in fabricating TiO₂ ceramic coating. This study showed that the process gas conditions are not a main factor in ceramic deposition cold spray process. Furthermore, their results prove that the microstructural and mechanical characteristics of feedstock powder are the key influencers of the deposition efficiency and properties of cold spray coating. However, the influence of starting powder as an important parameter for the formation of oxide material coating by CS is not yet well understood.

In the present study, two types of TiO₂ powder, nanopowder and submicron-sized sintered powder, were used as feedstocks in the deposition of nanostructured TiO₂ coating on aluminum substrate by cold spraying using nitrogen as the processing gas. The effect of the feedstock morphology on coating deposition was investigated. The morphology and crystal structure of the powders and microstructure of the coated samples were analyzed. In addition, some mechanical properties of coating, including adhesion strength and hardness distribution were evaluated.

Experimental Procedure

Materials

Two types of commercially available TiO₂ powder (Cosmo chemical, Korea) were used as the starting powder in the present study. Powder A was composed of nanocrystal particles and powder B was prepared through agglomerating ultra-fine particles, using polyvinyl alcohol as a binder. The agglomerated powder was tempered for 2 h at 800 °C in air atmosphere before spraying. An aluminum plate with dimensions of 100 mm × 30 mm × 1.5 mm was employed as a substrate for coating deposition. An average Vickers microhardness of 47.97 ± 1.2 HV was obtained for the substrate under a 100-g load. Prior to spraying, the substrate was rinsed with acetone. The chemical composition of the substrate was measured by

energy-dispersive x-ray (EDX) spectroscopy and is presented in Table 1.

Processing of Coating

A custom-built high-pressure cold spraying system was employed to deposit the coating. A spray gun with a converging–diverging de Laval-type nozzle with a 2-mm diameter throat, a 175-mm long diverging section, and an exit diameter of 5 mm was adopted. The substrate was moved by an X–Y drive system at a traverse speed of 20 mm/s during spraying in order to form a uniform thickness coating. Nitrogen gas was employed as both an accelerating gas and powder feeding gas, at a pressure of 1.5 and 1.6 MPa, respectively. The gas temperature in the prechamber was 500 °C. The standoff distance from the nozzle exit to the substrate surface was 35 mm.

Powders and Coating Characterization

X-ray diffraction was used to detect the phase and crystalline structure of the powders. XRD patterns were obtained using a Co- $k\alpha$ radiation ($\lambda = 1.78897 \text{ \AA}$) source at a setting of 40 mA and 40 kV (X'Pert MPD, Philips). XRD spectra were recorded by scanning 2θ in the range $10\text{--}90^\circ$. The average crystallite size of the TiO_2 powders was estimated using the XRD data and the Scherrer equation (Eq 1):

$$D = \frac{K\lambda}{\beta \cos\theta} \quad (\text{Eq 1})$$

where D is the crystallite size in nm, K is the shape constant (0.9), λ is the x-ray wavelength of Co- $k\alpha$ radiation in nm, θ is the Bragg's angle in degrees, and β is full width at half maximum (FWHM) of the diffraction peak and can be calculated by the Warren's formula (2).

$$B^2 = (B_m^2 - B_s^2) \quad (\text{Eq 2})$$

where B_m is broadening of the peak in the XRD pattern and B_s is broadening of the same peak obtained from XRD pattern of a standard bulk powder with crystallite size greater than $1 \mu\text{m}$ (Ref 31). The coated samples were prepared using cold mounting, grinding and fine polishing to achieve the desired surface. The powder morphology and cross-sectional microstructure of the granule powder and coating were observed by scanning electron

Table 1 Chemical composition of aluminum substrate in wt.%

Al	Si	Mg	Fe	Zn	Cu	Mn
Balance	1.79	0.5	0.41	0.38	0.26	0.09

microscope (SEM: Philips XL30) and field emission scanning electron microscopy (FESEM: MIRA3 TESCAN). The porosity of the granule powder and coating was determined using image processing from the cross-sectional SEM images. The surface roughness of the substrate before and after spraying was determined by field emission scanning electron microscope cross-sectional image. The microhardness of powder B was tested with a microhardness tester under a 100-g load for a loading time of 10 s, while the microhardness of the substrate was tested under a 100-g load for a loading time of 20 s. The adhesion between the coating and the Al substrate was evaluated by ultrasonic cleanout. The coating was put in a 185 W ultrasonic cleaner for 1 min. The adhesion was evaluated according to the spalling state of the coating.

Results and Discussion

Characterization of Feedstock Powder

XRD spectra of the starting powders are shown in Fig. 1. It can be seen that powder A has a single-phase anatase structure and powder B has both anatase and rutile phase structures. The existence of the rutile phase is due to the annealing process at 800 °C. The rutile content in powder B was calculated by using the diffraction intensity of rutile and anatase in the XRD pattern. The following equation was used to estimate the rutile content in powder B.

$$X_R = \frac{1}{1 + 0.8 \left(\frac{I_A}{I_R} \right)} \quad (\text{Eq 3})$$

where X_R is the rutile content in powder B, and I_A and I_R are the intensity of the anatase peak (101) and rutile peak (110), respectively, in the XRD pattern. Powder B was

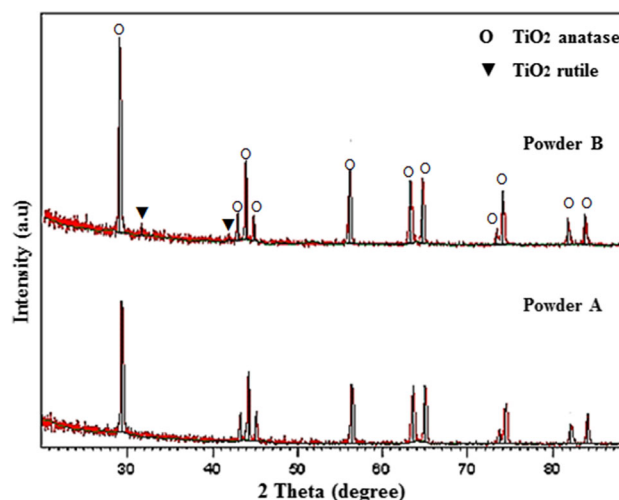


Fig. 1 The XRD spectra of feedstock powders

composed of 97.34% anatase phase and 2.66% rutile phase. It is obvious that the dominant crystal phase present in powder B after heat treatment is an anatase phase with tetragonal crystal structure. The crystallite sizes calculated using the Scherrer's equation were 34 nm and 40 nm for powders A and B, respectively. Heat treatment increases the crystallite sizes and crystallinity in TiO₂ powder.

The morphology and the size distribution of the powders A and B used as coating materials are shown in Fig. 2 and 3, respectively. The average particle sizes of the powders were measured from SEM images. Figure 2 reveals that powder A consists of spherical ultra-fine particles with a diameter of about 100 ± 15.3 nm. Figure 3 displays that powder B has an agglomerated structure consisting of very fine nanoparticles. The morphology of powder B is spherical, with a diameter of about 80 ± 11 μ m.

Figure 4 shows the cross-sectional SEM image of powder B. Nearly all particles in powder B exhibited a spherical morphology and porous microstructure. The measurement results showed that the powder's porosity is $\% 21 \pm 0.8$, and its microhardness is 17.5 ± 2.2 HV_{0.1}.

Characterization of Coating

Figure 5 shows a cross section of cold-sprayed TiO₂ coating deposited on aluminum substrate with powder A. It is clear that only a very thin coating is present on the substrate surface. The thickness of the coating is about 490 nm, and it was found that the coating thickness could not build up further due to starting powder characteristics. Powder A consists of fine nanoparticles that have a loosely agglomerated morphology. This uncontrolled agglomeration of nanoparticles is due to their high surface energy. Few of the spherical nanoparticles and irregular loose

agglomerate particles can cross through the bow shock layer near the substrate, due to their small size. Therefore, it seems that only around 10–20% of powder A was deposited on the substrate since a thicker ceramic coating did not build up.

Figure 6 shows the cross-sectional microstructure of the coating prepared with powder B. It is clear that continuous TiO₂ coating with a thickness of 15–20 μ m was deposited on the substrate surface. In comparison with Fig. 5, powder B formed a more defined and thicker coating. Detailed observation of the interface between coating and substrate shows no delamination and good adhesion. Most of the impacted particles stick to each other well and build up the coating. Although it is impossible for ceramic particles to deform under the impact of spray particles, the tamping effect will compact particles under high impact pressure. As a result, an apparently dense coating is formed with the successive deposition of spray particles.

It seems that both powder types were deposited under the same conditions, and there are no visible large pores and cracks, due to the tamping effect caused by the continuous impacts of particles. Apart from these similarities, the thickness of the coatings achieved with powders A and B differ, as shown in Fig. 5 and 6. That with powder B is 30 times thicker than that with powder A. Since the coating deposition parameters are same for both coatings, it seems that the starting powder characteristics caused this difference.

The differences between powders A and B during the cold spray process are explained next. As shown in Fig. 2 and 3, the particle size distributions of the two powders differ significantly, in turn significantly affecting the flow ability of the powders. As an example of the latter, powders typically exhibit poorer flow properties than coarse

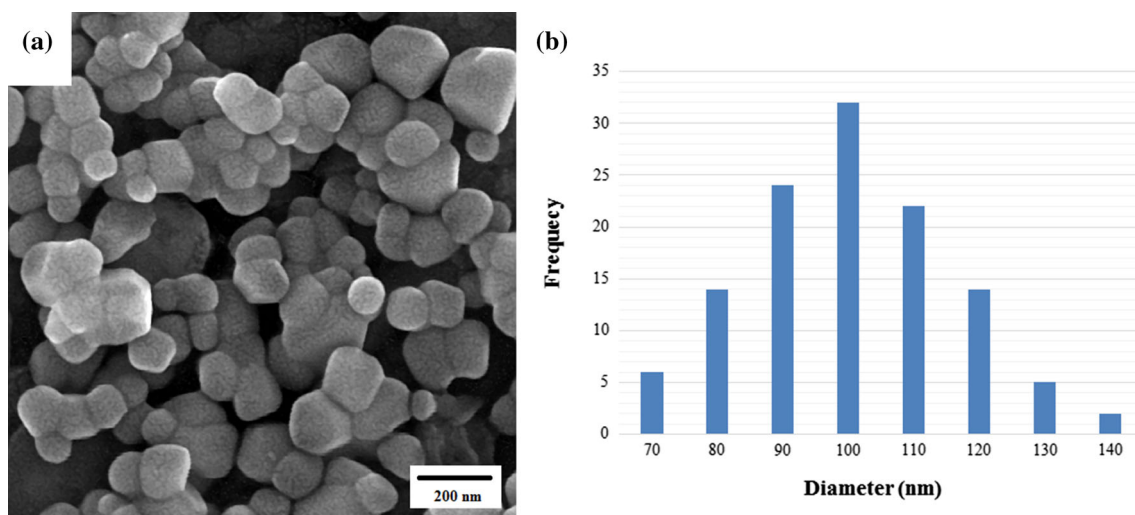


Fig. 2 Powder A characterization: (a) morphology of TiO₂ powder, (b) particle size distribution

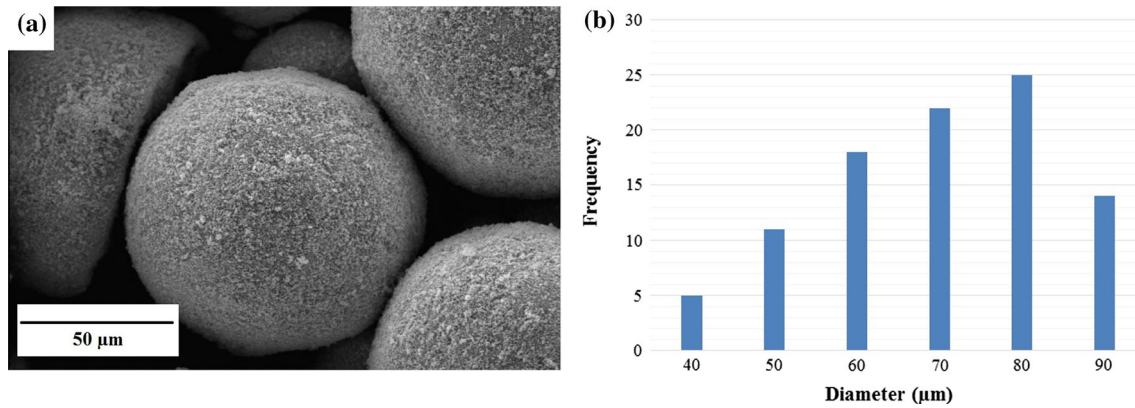


Fig. 3 Powder B characterization: (a) SEM micrograph, (b) particle size distribution

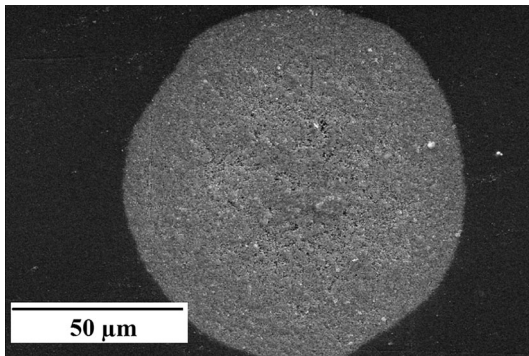


Fig. 4 Cross-sectional view of the powder B

particles or agglomerates. This agglomeration can be a valuable tool in improving the flow ability of powders. Therefore, powder B can be carried with N_2 gas and reach the substrate more easily than powder A.

Studies have shown that particle velocity has a strong effect on coating deposition. To reveal differences during deposition of the two powder types, the particle velocity for each powder was calculated by the formula mentioned

in Assadi et al.'s paper (Ref 32). Their formula considers the effect of various factors on particle velocity:

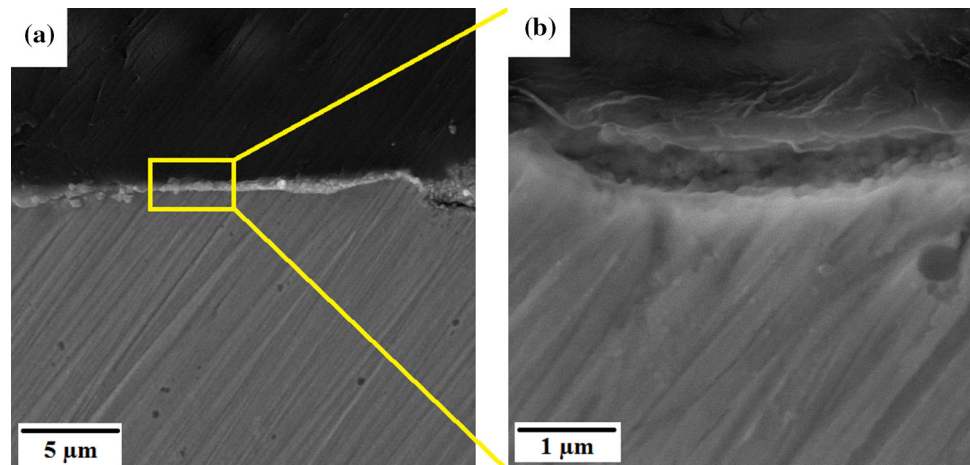
$$V_{pi} = V \left(1 + \frac{\rho_0 \delta}{\rho_p d_p} \right)^{-1} \quad (\text{Eq 4})$$

where V_{pi} is the impact velocity of particles, ρ_0 is gas stagnation density, δ is a fitting parameter of about 0.0007 m, ρ_p is particle density, d_p is particle diameter, and V is the approximated particle velocity at the nozzle exit, calculated as follows:

$$V = \left(\frac{c_2}{\sqrt{RT_0}} + \sqrt{\frac{\rho_p d_p}{C_d L_d p_0}} \right)^{-1} \quad (\text{Eq 5})$$

where c_2 is 0.42 for nitrogen, R is the universal gas constant, T_0 is the gas stagnation temperature, p_0 is the gas stagnation pressure, C_d is the drag coefficient, and L_d is length of the diverging (supersonic) part of the nozzle. According to Eq 4 and 5, V_{pi} is plotted as a function of particle sizes for powders A and B. Figure 7 shows the variation of impact velocity versus particle sizes for powder A and B. It is clear that the particle impact velocity, in

Fig. 5 FESEM micrograph of the TiO_2 coating deposited with powder A: (a) cross-sectional image, (b) zoom up image



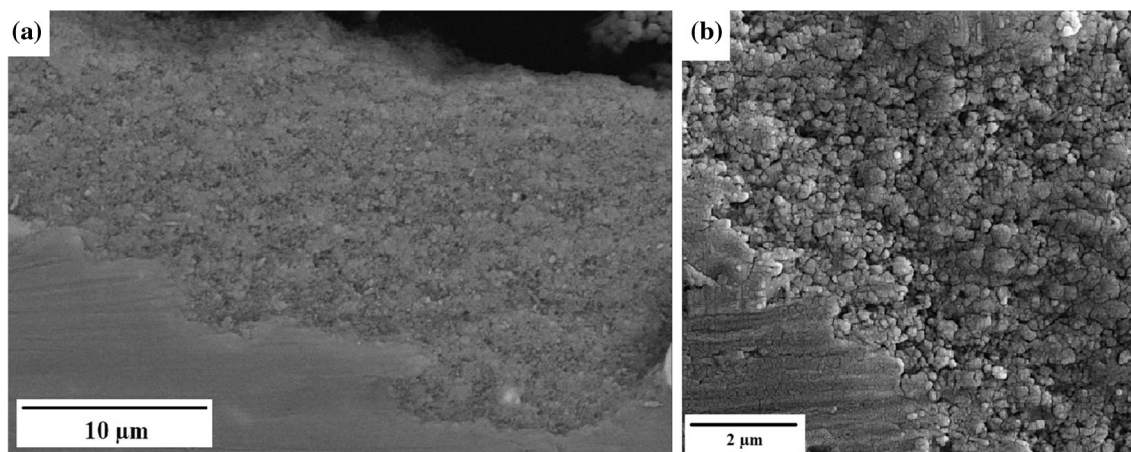


Fig. 6 Interface between the TiO₂ coating by powder B and Al substrate: (a) SEM images of cold-sprayed TiO₂ coating, (b) FESEM of interface

response to particle size, increases from 47 to 94 m/s for powder A and 450–563 m/s for powder B. For the average particle size of powder B, the average impact velocity is about 494 m/s, which is much higher than the impact velocity for powder A. In summary, powders with larger particles accelerate to a higher velocity and so are more easily deposited onto the substrate than the powders with smaller particle.

One of the important parameters that effect powder A spraying and its velocity is the bow shock layer. The bow shock has a negative influence on deposition efficiency as a result of reduced particle velocity. Powder A, due to its very small particles, has low kinetic energy and is significantly slowed by the bow shock layer. Therefore, in the CS process, powder A is deflected before it reaches the substrate. Gilmore et al. (Ref 33) and Hanft et al. (Ref 34) predicted that the smallest particles (< 5–15 μm) could be decelerated and even deflected away from the substrate by the bow shock. In conclusion, powder B, because of its agglomerate structure, has better flow ability and can pass through the bow shock layer and hit the substrate at high speed, but powder A, with its very small nanoparticles, cannot reach to the substrate at an appropriate velocity.

Based on the discussion above, powder B obtains high kinetic energies and hits the substrate at high velocity, leading to plastic deformation of the metallic substrate, associated with increased surface roughness. As shown in Fig. 8 and 9, the surface roughness increases significantly after cold spray deposition of powder B. This roughness causes mechanical entanglement that might also play an important role in the buildup stage (Ref 29). For brittle materials like ceramics, the first layer is achieved by plastic deformation of the ductile metallic substrate; i.e., the particles are embedded into the substrate without any additional binding agent or calcination procedure. Figure 9(b) shows that the coating/substrate interface is relatively rough when the particles hit the substrate at a high speed. As a result, titanium oxide particles embed in the Al substrate. Although the deposition mechanism of CS has not been understood well until now, but it is clear that the powder structure and properties are crucial for the preparation of the desired coating.

The porosities of powder B and the TiO₂ coating were measured using cross-sectional SEM images. Image analyzer results show powder B and the TiO₂ coating porosities as %21.5 ± 0.8 and %12.7 ± 1.6, respectively.

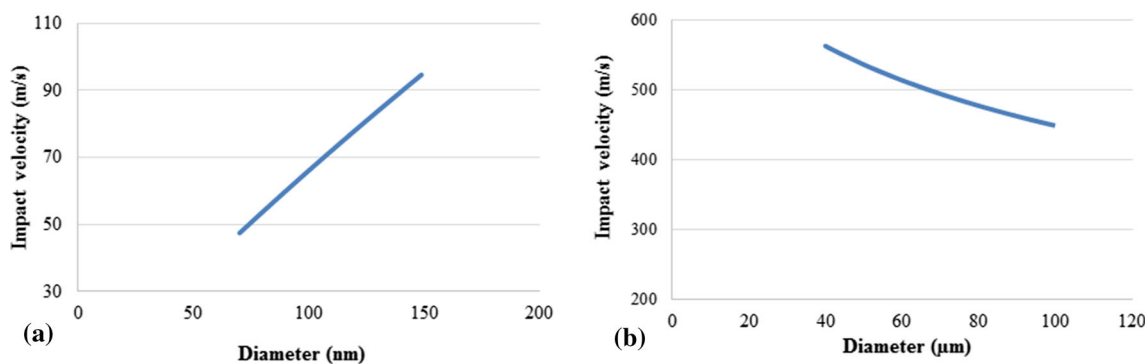


Fig. 7 Variation of the particle impact velocity for powder A (a) and powder B (b)

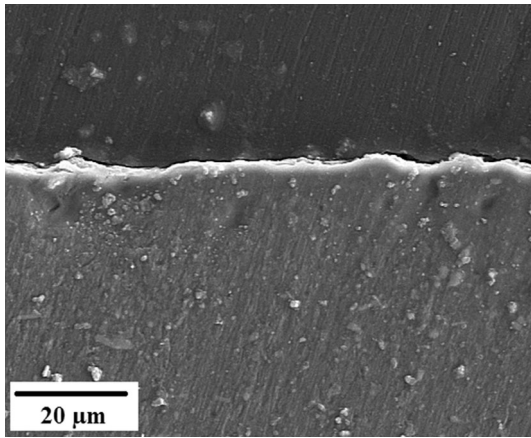


Fig. 8 Surface roughness of the Al substrate before coating

Compared to the initial powder, the coating has lower porosity. Subsequent impacts of other particles may have partly lessened the porosity of the coating by hammering the previously deposited particles into the substrate.

Figure 10(a) and (b) shows the surface morphology of the coating before and after ultrasonic cleaning, respectively. For the coatings deposited with powder B, no spalling of the fabricated coating occurred to the sample.

The coating shows good enough adhesion with the substrate as well as good cohesion within the coating. The boundaries between the particles become ambiguous in both the surface and cross section (Fig. 6a), suggesting that strong particle/particle bonding occurred in the coating with powder B.

Conclusions

Differences during the deposition of titanium oxide coating were investigated using two different powder types, nano-TiO₂ powders and agglomerated powders. Better particle/substrate bonding and buildup continuous ceramic coating were observed for the agglomerate submicron powder. The key to this result is attributed to the particle velocity differences during cold spray that affected by two competing mechanisms outside of the nozzle during CS. Both powders accelerate due to the free gas jet outside of the nozzle; however, the presence of the bow shock, which exists a short distance from the substrate, theoretically reduces the nano-TiO₂ powders velocity. The agglomerate TiO₂ powders pass through the bow shock layer and impact the substrate at high velocities. In this case, the substrate is

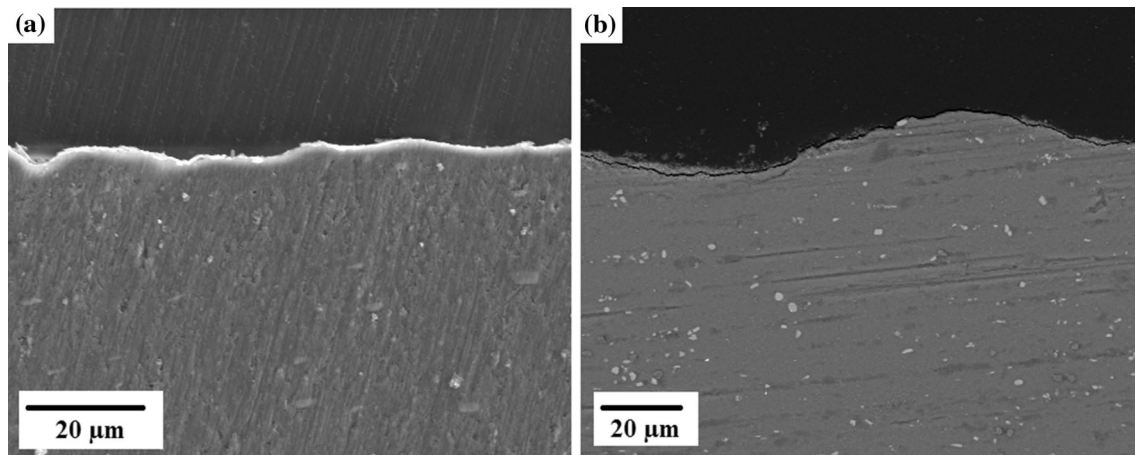


Fig. 9 Surface roughness of the Al substrate after cold spray process with; (a) powder A, (b) powder B

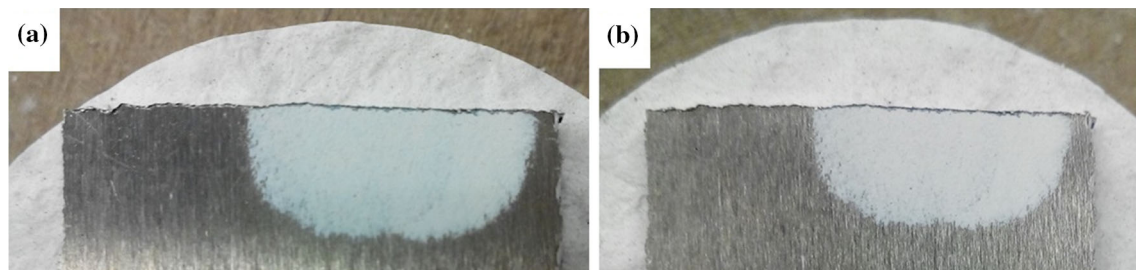


Fig. 10 Surface morphologies of the coatings by powder B (a) As-deposited layer, (b) after ultrasonic cleaning for 60 s

deformed due to high impact velocities of the agglomerate powders and continuous TiO₂ coating with a thickness of 15–20 μm with a good enough adhesion to the substrate was deposited. In addition, the porosity of the TiO₂ agglomerate powder may lead to the breaking down of the particles when impacting the substrates. Then, the crystals are decoupled and their newly unstable surfaces bond to other counterparts, creating more stable interfaces, which allows for the bonding of the newly impacting particles and thus the buildup of the coating. In conclusion, through optimization of the powder structure, the properties of cold-sprayed ceramic coating can be improved and tailored for better performance.

References

1. F. Gärtner, T. Stoltenhoff, T. Schmidt, and H. Kreye, The Cold Spray Process and Its Potential for Industrial Applications, *J. Therm. Spray Technol.*, 2006, **15**(2), p 223–232
2. N. Bala, H. Singh, J. Karthikeyan, and S. Prakash, Cold Spray Coating Process for Corrosion Protection: A Review, *Surf. Eng.*, 2014, **30**(6), p 414–421
3. S. Grigoriev, A. Okunkova, A. Sova, P. Bertrand, and I. Smurov, Cold Spraying: From Process Fundamentals Towards Advanced Applications, *Surf. Coat. Technol.*, 2015, **268**, p 77–84
4. R. Ghelichi, D. MacDonald, S. Bagherifard, H. Jahed, M. Guagliano, and B. Jodoin, Microstructure and Fatigue Behavior of Cold Spray Coated Al5052, *Acta Mater.*, 2012, **60**(19), p 6555–6561
5. V.K. Champagne and D. Helfritsch, Critical Assessment 11: Structural Repairs by Cold Spray, *J. Mater. Sci. Technol.*, 2015, **31**(6), p 627–634
6. A. List, F. Gärtner, T. Mori, M. Schulze, H. Assadi, and S. Kuroda, Cold Spraying of Amorphous Cu₅₀Zr₅₀ Alloys, *J. Therm. Spray Technol.*, 2015, **24**(1–21), p 108–118
7. J. Henao, A. Concustell, I.G. Cano, N. Cinca, S. Dosta, and J.M. Guilemany, Influence of Cold Gas Spray Process Conditions on the Microstructure of Fe-Based Amorphous Coatings, *J. Alloys Compd.*, 2015, **622**, p 995–999
8. S. Dosta, G. Bollelli, A. Candeli, L. Lusvardi, I.G. Cano, and J.M. Guilemany, Plastic Deformation Phenomena During Cold Spray Impact of WC-Co Particles Onto Metal Substrates, *Acta Mater.*, 2017, **124**, p 173–181
9. S.A. Alidokht, P. Vo, S. Yue, and R.R. Chromik, Cold Spray Deposition of Ni and WC-Reinforced Ni Matrix Composite Coatings, *J. Therm. Spray Technol.*, 2017, **26**(8), p 1908–1921
10. J. Freitag and D.W. Bahnemann, Evaluation of the Photocatalytic (Visible-Light) Activity of Cold Gas Sprayed TiO₂ Layers on Metal Sheets, *Phys. Status Solidi*, 2014, **8**(6), p 596–599
11. W. Wong, E. Irissou, A.N. Ryabinin, J.G. Legoux, and S. Yue, Influence of Helium and Nitrogen Gases on the Properties of Cold Gas Dynamic Sprayed Pure Titanium Coatings, *J. Therm. Spray Technol.*, 2011, **20**(1–2), p 213–226
12. K.H. Ko, J.O. Choi, and H. Lee, Characteristics of Cold Sprayed Dendritic Cu Coatings, *Surf. Eng.*, 2016, **32**(9), p 650–654
13. G. Huang, H. Wang, X. Li, L. Xing, and J. Zhou, Deposition Efficiency of Low Pressure Cold Sprayed Aluminum Coating, *Mater. Manuf. Process.*, 2018, **23**(10), p 1100–1106
14. M. Diab, X. Pang, and H. Jahed, The Effect of Pure Aluminum Cold Spray Coating on Corrosion and Corrosion Fatigue of Magnesium (3% Al-1% Zn) Extrusion, *Surf. Coat. Technol.*, 2017, **309**, p 423–435
15. R. Drehmann, T. Grund, T. Lampke, B. Wielage, C. Wustefeld, M. Motylenko, and D. Rafaja, Essential Factors Influencing the Bonding Strength of Cold Sprayed Aluminum Coatings on Ceramic Substrates, *J. Therm. Spray Technol.*, 2018, **27**(3), p 446–455
16. A. Ganesan, M. Yamada, and M. Fukumoto, Cold Spray Coating Deposition Mechanism on the Thermoplastic and Thermosetting Polymer Substrates, *J. Therm. Spray Technol.*, 2013, **22**(8), p 1275–1282
17. S.B. Dayani, S.K. Shaha, R. Ghelichi, J.F. Wang, and H. Jahed, The Impact of AA7075 Cold Spray Coating on the Fatigue Life of AZ31B Cast Alloy, *Surf. Coat. Technol.*, 2018, **337**, p 150–158
18. G. Shayegan, H. Mahmoudi, R. Ghelichi, J. Villafuerte, J. Wang, M. Guagliano, and H. Jahed, Residual Stress Induced by Cold Spray Coating of Magnesium AZ31B Extrusion, *Mater. Des.*, 2014, **60**, p 72–84
19. W. Li, H. Assadi, F. Gaertner, and S. Yin, A Review of Advanced Composite and Nanostructured Coatings by Solid-State Cold Spraying Process. *Crit. Rev. Solid State Mater. Sci.* (2018). <https://doi.org/10.1080/10408436.2017.1410778>
20. S. Yin, X. Wang, X. Suo, H. Liao, Z. Guo, W. Li, and C. Coddet, Deposition Behavior of Thermally Softened Copper Particles in Cold Spraying, *Acta Mater.*, 2013, **61**(14), p 5105–5118
21. M. Hassani-Gangaraj, D. Veysset, V.K. Champagne, K.A. Nelson, and C.A. Schuh, Adiabatic Shear Instability is Not Necessary for Adhesion in Cold Spray, *Acta Mater.*, 2018, **158**, p 430–439
22. H. Assadi, H. Kreye, F. Gärtner, and T. Klassen, Cold Spraying—A Materials Perspective, *Acta Mater.*, 2016, **116**, p 382–407
23. H.J. Kim, C.H. Lee, and S.Y. Hwang, Superhard Nano WC-12%Co Coating by Cold Spray Deposition, *Mater. Sci. Eng. A*, 2005, **391**, p 243–248
24. K. Kim, M. Watanabe, and S. Kuroda, Bonding Mechanisms of Thermally Softened Metallic Powder Particles and Substrates Impacted at High Velocity, *Surf. Coat. Technol.*, 2010, **204**(14), p 2175–2180
25. A. Moridi, S.M. Hassani-Gangaraj, M. Guagliano, and M. Dao, Cold Spray Coating: Review of Material Systems and Future Perspectives, *Surf. Eng.*, 2014, **36**(6), p 369–395
26. R. Ballhorn, F. Peterka, H. Kreye, I. Burlacov, T. Stoltenhoff, and J. Jirkovsky, *Production of Photocatalytically Active Polymer Surfaces of Variable Composition Comprises Cold Gas Spraying them with Oxide Powder to Produce Adherent Photocatalytic Layer*, German Patent Number: DE102004038795A1 (2004)
27. T. Klassen and J.A. Kliemann, *Method for Manufacturing a Photocatalytically Active Layer*, United States Patent US2007148363A1 (2007)
28. G.J. Yang, C.J. Li, F. Han, W.Y. Li, and A. Ohmori, Low Temperature Deposition and Characterization of TiO₂ Photocatalytic Film Through Cold Spray, *Appl. Surf. Sci.*, 2008, **254**, p 3979–3982
29. J.O. Kliemann, H. Gutzmann, F. Gärtner, H. Hübner, C. Borchers, and T. Klassen, Formation of Cold-Sprayed Ceramic Titanium Dioxide Layers on Metal Surfaces, *J. Therm. Spray Technol.*, 2011, **20**(1–2), p 292–298
30. M. Yamada, H. Isago, H. Nakano, and M. Fukumoto, Cold Spraying of TiO₂ Photocatalyst Coating With Nitrogen Process Gas, *J. Therm. Spray Technol.*, 2010, **19**(6), p 1218–1223
31. M. Mozaffari, J. Amighian, and E. Darsheshdar, Magnetic and Structural Studies of Nickel-Substituted Cobalt Ferrite Nanoparticles, Synthesized by the Sol–Gel Method, *J. Magn. Mater.*, 2014, **350**, p 19–22
32. H. Assadi, T. Schmidt, H. Richter, J.O. Kliemann, K. Binder, F. Gärtner, T. Klassen, and H. Kreye, On Parameter Selection in

- Cold Spraying, *J. Therm. Spray Technol.*, 2011, **20**(6), p 1161-1176
33. D.L. Gilmore, R.C. Dykhuizen, R.A. Neiser, M.F. Smith, and T.J. Roemer, Particle Velocity and Deposition Efficiency in the Cold Spray Process, *J. Therm. Spray Technol.*, 1999, **8**(4), p 576-582
34. D. Hanft, J. Exner, M. Schubert, T. Stöcker, P. Fuierer, and R. Moos, An Overview of the Aerosol Deposition Method: Process Fundamentals and New Trends in Materials Applications, *J. Ceram. Sci. Technol.*, 2015, **6**(3), p 147-182